We are IntechOpen,
the world's leading publisher of
Open Access books
Built by scientists, for scientists

6,900
Open access books available

186,000
International authors and editors

200M
Downloads

154
Countries delivered to

Our authors are among the

TOP 1%
most cited scientists

12.2%
Contributors from top 500 universities

BOOK CITATION INDEX
CLARIVATE ANALYTICS
INDEXED

WEB OF SCIENCE™

Selection of our books indexed in the Book Citation Index
in Web of Science™ Core Collection (BKCI)

Interested in publishing with us?
Contact book.department@intechopen.com

Numbers displayed above are based on latest data collected.
For more information visit www.intechopen.com

Chapter

Reflectance Spectra Analysis Algorithms for the Characterization of Deposits and Condensed Traces on Surfaces

Ran Aharoni, Asaf Zuck, David Peri and Shai Kendler

Abstract

Identification of particulate matter and liquid spills contaminations is essential for many applications, such as forensics, agriculture, security, and environmental protection. For example, toxic industrial compounds deposition in the form of aerosols, or other residual contaminations, pose a secondary, long-lasting health concern due to resuspension and secondary evaporation. This chapter explores several approaches for employing diffuse reflectance spectroscopy in the mid-IR and SWIR to identify particles and films of materials in field conditions. Since the behavior of thin films and particles is more complex compared to absorption spectroscopy of pure compounds, due to the interactions with background materials, the use of physical models combined with statistically-based algorithms for material classification, provides a reliable and practical solution and will be presented.

Keywords: diffuse scattering, remote sensing, spectroscopy, surfaces, detection, mid wave infra-red, short wave infra-red, classification

1. Introduction

Spectroscopy is one of the foremost and main methods of characterizing materials of various states of matter—gas, liquid, solid, vapor, and aerosol. The need to remotely detect and identify residues, traces, contaminations, and small amounts of chemicals plays an important role in many fields, such as forensics and security [1], agriculture [2], food quality pharmaceuticals industry, climate research, and others.

Detection of surface contaminations and residues in a standoff manner enables scanning surface from a safe distance and with no physical contact with the sample, which may be hazardous or too sparse to necessitate wiping large area. Therefore, optical sensing can provide an immediate result, and it is favored over surface sampling techniques such as mass spectrometry techniques. Several studies and efforts utilizing probing techniques for ion-mobility spectrometry of explosives form surfaces through surface wiping [3] plasma ionization [4], desorption electrospray ionization from skin [5], and more. Non-contact preconcentration and ionization sampling methods, such as airflow-assisted ionization [6] and laser-induced breakdown spectroscopy [7], enable standoff detection of surface absorbed

chemicals. For further reading on sampling techniques and explosive detection, refer to Tourné's review [8].

Fourier-transform infrared (FTIR) spectroscopy, coupled with attenuated total reflection (ATR), can be used to probe trace amounts of spores [9] or other particles on solid surfaces [10], or remotely by imaging [11, 12]. Active methods for powders detection, in which the investigated sample is artificially illuminated rather than using ambient light, were also applied in various spectral regions, such as THz [13, 14], but more commonly in lower wavelengths. The mid-IR region, the most common for chemical spectroscopy, was pushed forward by developing the quantum cascade laser (QCL) [15, 16]. Laser-assisted spectroscopy for explosive detection, and other particulated matters, was also employed by various optical techniques, such as photo-acoustics [1, 17, 18]. Using near-field optical microscopy, Craig et al. scanned surfaces with condensed residues by scanning QCL with a rapid acquisition time of 90 s per spectrum [19]. Explosive's particles and residues using scanning QCL microscopic hyperspectral imaging enabled a four-second acquisition time [20]. Advancing technology provides the means for an even shorter detection time in the range of <0.1 s per spectral cube of trace surface contaminants [21]. A similar method, i.e., imaging the diffusely scattered radiation from a light source, was also demonstrated using a CO_2 laser [22]. The short wavelength of the IR region was also used for screening envelopes for traces of hazardous powders by hyperspectral imaging [23]. Multispectral imaging in the visible range was demonstrated for the detection and discrimination of bloodstains on cotton [24].

IR spectroscopy in the 7–14 μm band, i.e., mid-wave IR (MWIR, also termed long-wave IR; LWIR), is discussed in the first section of this chapter. This spectral region is used for inspecting molecular chemical information for gaseous and condensed matter. In condensed samples, MWIR spectroscopy is an analytical technique fitted for trace analysis, but it is non-penetrating, which can be affected by the surface morphology that scatters the light and affects the resulted spectrum. Short IR wavelengths (SWIR, 1–2.5 μm) spectroscopy, addressed in the second section of this chapter, is characterized by weaker absorption and larger penetration depth, resulting in diffuse reflection, allowing deeper investigation of the sample and revealing its physical and chemical structure. This is not an analytical method but provides information not only on the sample's surface but also on the sample's core compound and structure.

This chapter is divided into two main sections. The first section elaborates the issues of MWIR spectroscopy of surfaces and suggests a practical solution based on a physical model. The second part confronts the challenges of using SWIR for similar purposes and proposes a solution based on statistical learning.

2. Reflection and scattering: MWIR

The MWIR region, known as the 'molecular fingerprint region', reflects the molecular composition of most chemicals vib-rotational transitions, hence reviling the molecular structure by its unique spectral fingerprint. Due to its analytical capabilities, it was favored by spectroscopists for the investigation of the chemical properties of organic materials, and detection and identification needs. Acquiring spectrum for gaseous samples is quite straightforward—launching an optical beam through the sample results in spectral attenuation, i.e., absorbance, caused by the molecular transitions. The absence of back reflection is due to the lack of specific boundaries between materials with different refractive indices (n_1 and n_2). However, in a condensed matter, where the boundaries between materials are well defined such as in layers and particles, interference scattering and diffraction effect

the spectral scattering. Each of the following phenomena: interference, diffraction, and scattering, has its theory models and approximations that describe an interaction of light and matter. In fact, these three phenomena are manifestations of maxwell's equations, differ only by mathematical approximations, and therefore provide ambiguous results at certain conditions.

The simplest case is the reflection from a uniform layer, explained and demonstrated in the following sub-section, which has an exact solution and can be expanded to cases of non-uniform layers, such as traces and residues, as depicted in **Figure 1**. The upper figure illustrates a light beam that is specularly reflected from a flat layer. The lower figure presents a surface with residual contamination, which results in diffuse reflection. The lower figure presents the illumination of a contaminated surface. The surface is tilted such as the specular reflection component (in red), which can be orders of magnitude stronger than the diffuse reflection component, is directed away from the detector. Part of the diffuse reflection lobe, which originates mainly from residual traces, is directed to the detector (blue). This section explores the physics of MWIR reflection from a uniform and non-uniform coverage of surfaces and suggests methods for detecting and identifying traces and residues.

2.1 Uniform layers: general

As mentioned, the reflection of light from surfaces can be generally divided into specular reflection and diffuse reflection components, both illustrated in **Figure 1**.
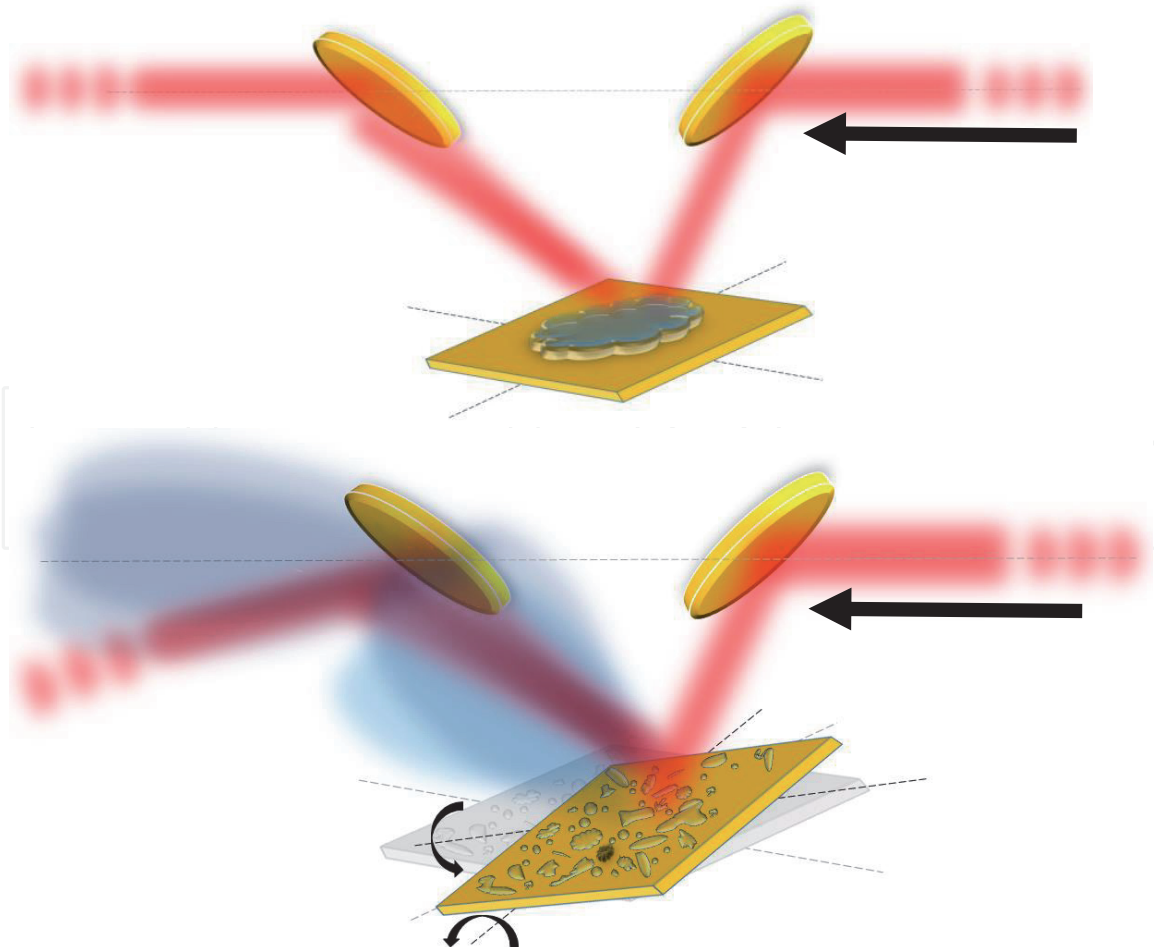
Figure 1.
Reflected light from residuals on a surface. The upper panel illustrates a uniform layer deposited on a surface and its specular reflection. The lower panel illustrates drops, particles and residuals on a surface and the diffuse reflection measurement. The black arrows represent the incident light direction.

The upper panel of the figure presents specular reflection from a finite layer, where the reflected light is directed to a detector. In thick and highly absorbing layers, the measured spectral reflection is comprised exclusively by the layer's molecular properties, i.e., the absorption coefficient and refractive index as described by Fresnel equation [25]. When the absorption coefficient and the thickness (and the light coherence length) allow the substantial optical intensity to be back-reflected from the carrying surface and complete at least one round trip, interference effects are observed, as illustrated in **Figure 2**. The figure illustrates the tracing of an optical field hitting a finite smooth layer with incidence angle θ. The multiple reflections and refractions amplitudes are summed up and then squared to get the light intensity. Almost no surface is smooth enough to avoid the scattered diffuse reflection lobe (illustrated in **Figure 1** lower panel). This component, which obeys the Lambertian reflection law with highly rough surfaces, is much weaker and negligible for relatively smooth surfaces. In cases of a partial cover of a surface by an analyte, it is desired to avoid the specular reflection, which might be orders of magnitude stronger than the diffuse reflection of the analyte traces and therefore mask it, as illustrated in **Figure 1b** and discussed in Section 2.3.

Figure 2 refers to the scenario illustrated in **Figure 1a**, and presents detailed optical ray tracing through a finite and uniform thickness layer. An optical beam is hitting a uniform interface of a transparent layer with parallel facets at incidence angle Θ. Inside the layer, the optical field suffers multiple internal reflections, which give rise to interference. The reflection of a non-absorbing layer is:

$$R = \frac{\left(\sqrt{R_1} - \sqrt{R_2}\right)^2 + 4\sqrt{R_1}\sqrt{R_2}\sin^2(\delta/2)}{\left(1 - \sqrt{R_1}\sqrt{R_2}\right)^2 + 4\sqrt{R_1}\sqrt{R_2}\sin^2(\delta/2)} \tag{1}$$

where R_1 and R_2 are the intensity reflection coefficient from the facets (calculated by Fresnel relations) and the optical phase is $\delta = 2\pi n_{(\lambda)}L\cos(\Theta)/\lambda$ for a layer with thickness L. It is clear that unlike absorption spectroscopy, which measures the attenuation directly, the interference described in Eq. (1) has a crucial impact on the reflected spectra. Generalizing Eq. (1) to the case of semi-absorbing material, for example, a nonvolatile liquid over a glass window, ceramic tile, metallic surface, or other casual flat surfaces, results in the following equation:
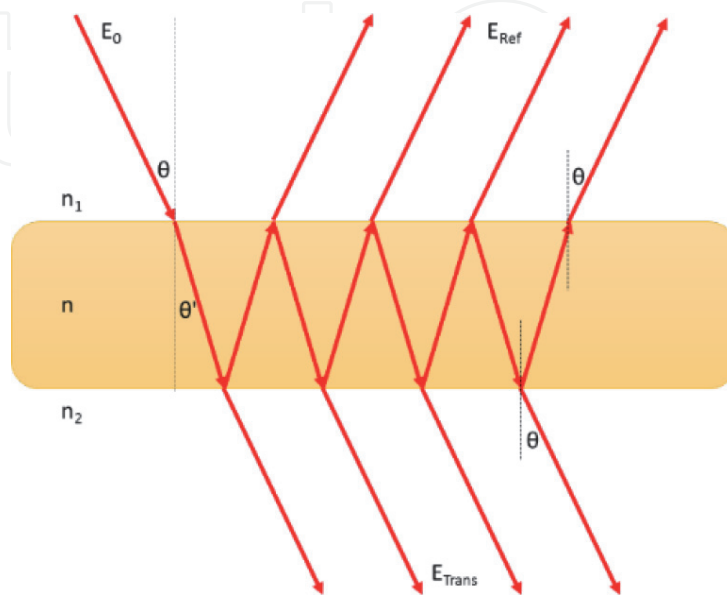

Figure 2.
Ray tracing of a finite uniform layer. E_o, E_{Ref}, E_{Trans} are the incident, reflected, and transmitted fields, respectively.

$$R = \frac{\left(\sqrt{R_1} - \sqrt{R_2}e^{\alpha L\cos(\theta)}\right)^2 + 4\sqrt{R_1}\sqrt{R_2}e^{\alpha L\cos(\theta)}\sin^2(\delta/2)}{\left(1 - \sqrt{R_1}\sqrt{R_2}e^{\alpha L\cos(\theta)}\right)^2 + 4\sqrt{R_1}\sqrt{R_2}e^{\alpha L\cos(\theta)}\sin^2(\delta/2)} \qquad (2)$$

where α is the attenuation coefficient defined as $4\pi k_{(\lambda)}/\lambda$ (λ is the wavelength, and $k_{(\lambda)}$ is the imaginary part of the refractive index), thus, the reflected spectrum is affected heavily by the layer thickness, as seen in **Figure 3**, showing the absorption of Polymethyl Methacrylate (PMMA) layer, and reflected spectrum from different layers of it. The inset of the figure shows the absorption coefficient, measured with ATR. The figure shows reflectance measurements of three different spin-coated layers of PMMA, measured with a spectrally scanning laser, according to the set-up depicted in **Figure 1**. The measured spectra cannot be precisely associated with the absorption coefficient, from the reasons described above (Eq. (2)). Significant differences between the three layers can be seen as the peak's location are shifts and change their shape. This figure accentuates the resulted differences of reflected spectra from the same material with different morphology (i.e., layer thickness). The thickness differences are just a few microns (layers thicknesses are 16, 20, 27 μm), indicated by low correlations of the measured signatures, as shown in the table given in the below figure.

2.2 Uniform layers: experimental implementation

As explained above, by knowing the optical properties of the layer and the carrying surface, one can calculate the reflected spectrum, using Eq. (2). This is exemplified in **Figure 4**, showing the real and imaginary parts of the refractive index of poly-dimethyl-siloxane (PDMS) on a metallic surface (**Figure 4a**), and the measured spectral reflection from 0.63 μm to 22 μm layers (**Figure 4b** and **c**). **Figure 4a** presents the measured ATR spectra of PDMS, where the refractive index (n) is calculated by Kramers-Kronig relations [26]. **Figure 4b** presents the reflected
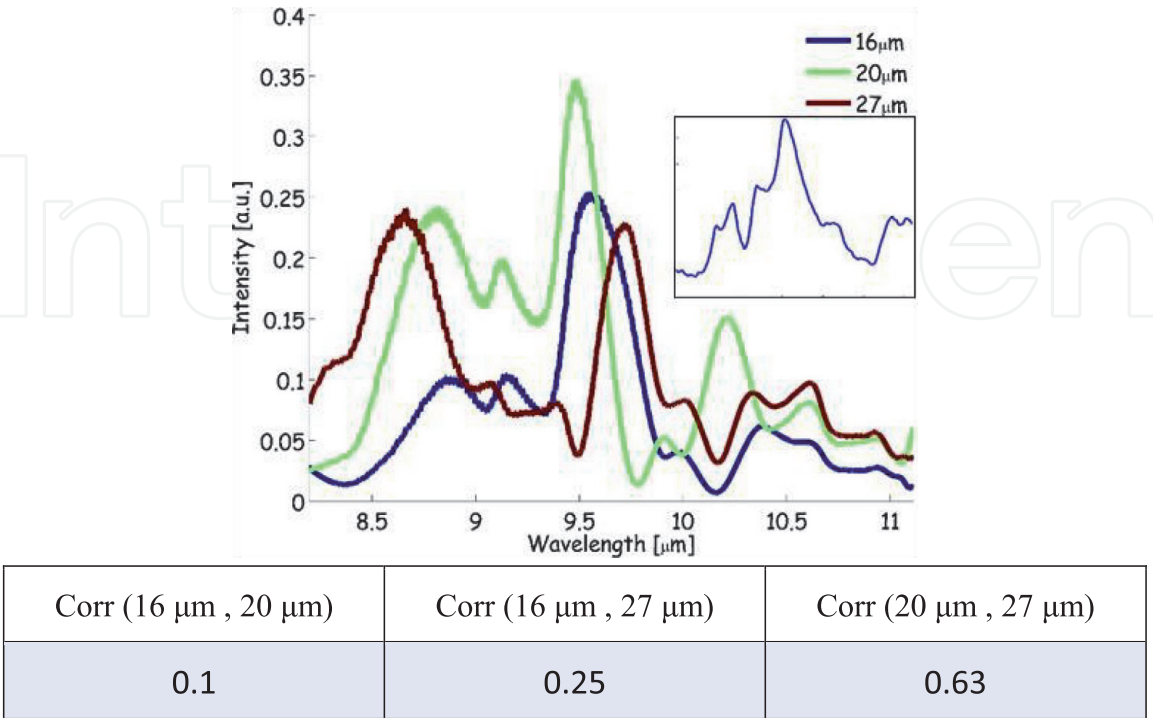

Corr (16 μm , 20 μm)	Corr (16 μm , 27 μm)	Corr (20 μm , 27 μm)
0.1	0.25	0.63

Figure 3.
Reflected spectra of PMMA layers. The inset depicts the absorption coefficient, and the three curves of the figure represent the reflected intensity from three different uniform layers. The table represents the correlation coefficients between the layers.
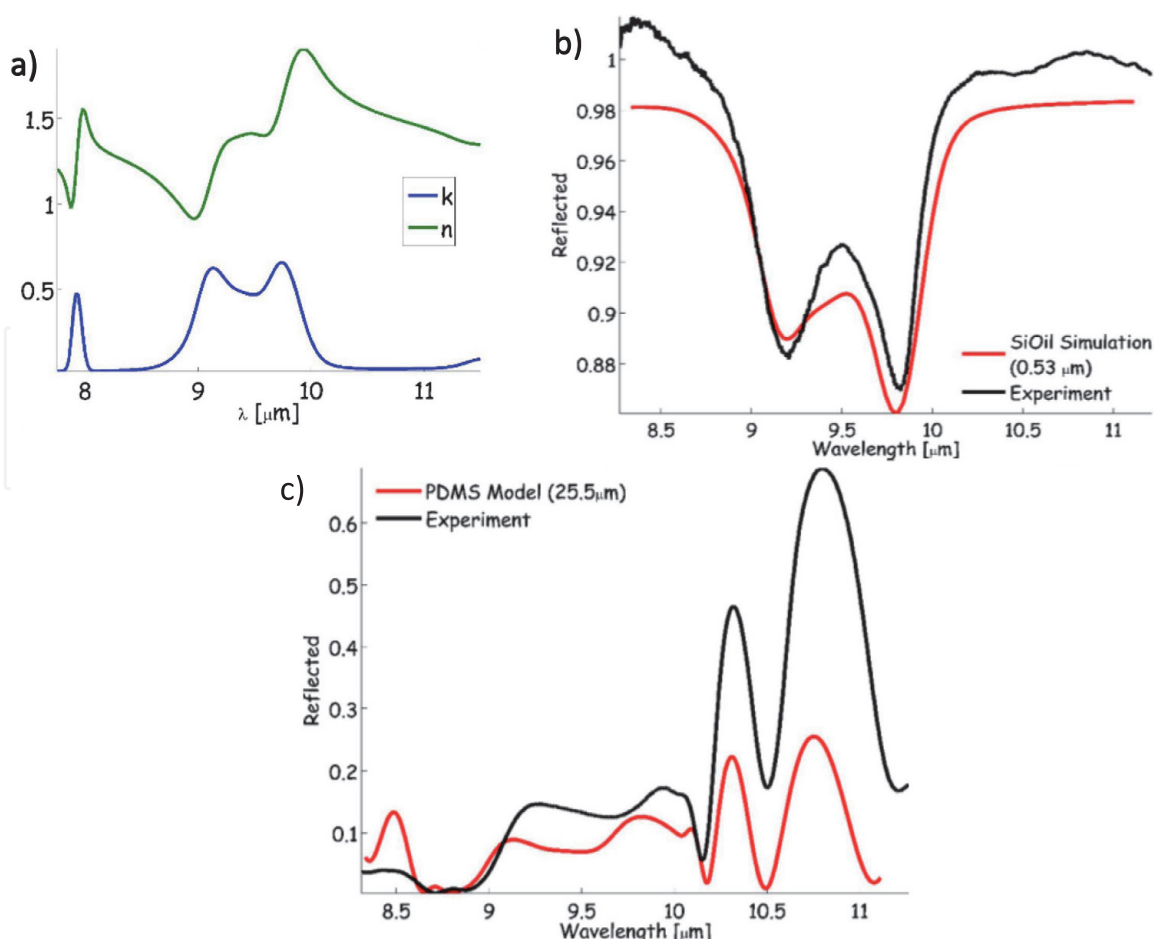
Figure 4.
PDMS layers reflection spectrum. (a) Optical properties (n is calculated). (b) Thin layer. (c) Thick layer.

spectrum of a thin layer that matches the absorption coefficient 'k' from **Figure 4a**. This layer is too thin compared to the wavelength, therefore interference effects are not observed, and the reflected spectrum correlates well with the absorption coefficient. **Figure 4c** presents the reflected spectrum from a layer having thickness more than twice the average wavelength. Consequently, an interference pattern appears at the edges of the acquired spectrum, where the absorption is negligible. Also, some deformation of the absorption around 9.5 μm is noticed. The interference fringes properties can be used for exact evaluation of the layer thickness by Eqs. (1) or (2)—the spacing between adjacent peaks (called 'free spectral range') is affected by the wavelength, thickness, incidence angle, and the refractive index, which are the components of the phase parameter δ from Eqs. (1) and (2). For a more accurate solution, one should account for the variation in the Snell law for absorbing medium interface, which may affect the form of Eq. (2) [27].

2.3 Non-uniform layers: diffraction and scattering

Disseminating liquid materials more efficiently can be achieved by spraying and drizzling, which cover larger areas with drops or droplets. Such dispersal processes usually result in size distribution similar to lognormal [28], which can be very wide and with standard deviation spread from a few microns to hundreds of microns. The size distribution of sprayed droplets has an important effect on the performance of agrochemical systems [29] and combustion engines [30] etc., mainly characterized by scattering and diffraction measurements of levitating particles. Mostly, the efforts are towards covering large volumes and surfaces with droplets for the highest efficiency of dissemination and surface coverage. The results are

similar to the lower panel of **Figure 1**, illustrating residuals and traces on a planar surface. The surface is tilted to avoid the specular reflection component that might mask the diffuse reflection component, which can be orders of magnitude weaker.

Light scattering is an extensive and well understood physical phenomenon, originating from Maxwell equations in the form of the wave equation [31], and depends on many factors such as the wavelength of light, incidence angle, material properties of the scatterer (absorption and refraction), and geometric factors of scatterers and illumination. As such, many scattering theories and models were developed, each describes these phenomena under different conditions and assumptions. For example: (1) Mie theory (full name: Lorenz-Mie-Debye theory) describes general scattering by homogeneous, isotropic spheres with no size limits but is more commonly used where the scatterer size is comparable to the light wavelength [32], and have many further approximations for different sizes and shapes of scattering particles. (2) Rayleigh scattering theory (Rayleigh-Gans-Debye) describes scattering from particles smaller than the wavelength [33], and more. In cases where the dissemination process, and hence the resulting size distribution, is unknown, it is unclear how to choose the most suitable approximation. Moreover, in liquid spray sediment over a surface, the interaction between the surface and the droplets may dramatically change the size and geometry of the droplets, and each scattering model might result in a different solution. We should note that most of the interactions of light with matter are fundamentally the same, and all are described by Maxwell's equations. More specifically, interference is a basic outcome of these equations, and it is the cause of diffraction and scattering, which are all different manifestations of light interaction with matter, and the only difference is the approximation of different theories. Therefore, it is expected that scattering by a sphere and reflection by a slab are similar [34, 35]. Accordingly, it will be demonstrated that the above-presented layers model (LM) can be used in many realistic scenarios for the detection and identification of sprayed liquid on a surface. Similarly, it is suggested that unknown condensed residuals on a surface can be detected, identified, and quantified by a simple reflection model instead of a complicated specific scattering model.

Figure 5 presents measured and calculated diffuse reflection normalized spectra of PDMS, the solid black spectra were calculated using the LM presented in the previous section, and the red dashed curves represent measure spectra of laboratory
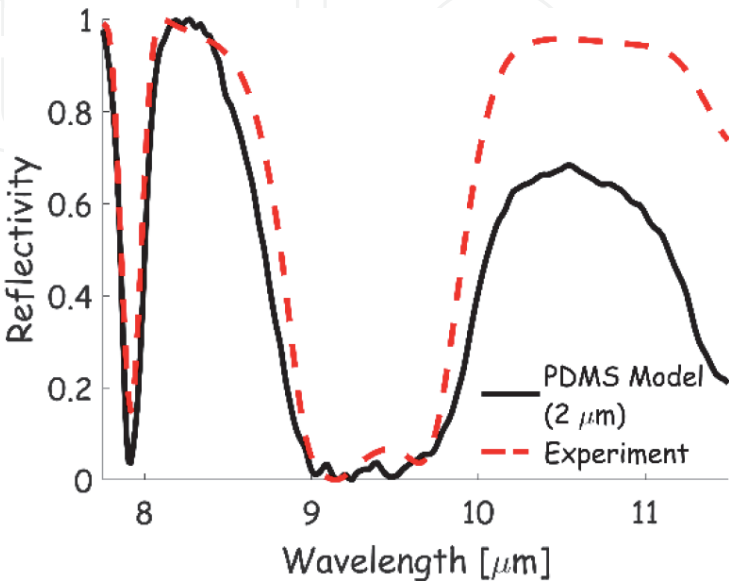

Figure 5.
Diffuse reflection measurement (solid black) of PDMS spray-on metalic surface, vs. LM (dashed red) (from [36]).

experiment, where PDMS was sprayed on a metallic surface and measured with EC-QCL, using the apparatus of in **Figure 1**. The droplet's size distribution was between a few microns and dozens of microns, where the majority was 10 microns and less. To resolve the thickness parameter (L) for the LM (see Eq. (2), where $\delta = \delta(\lambda)$), the LM was calculated repeatedly for all the desired thickness range and correlated to the experimental results, while the best correlation is presented in the figure. Non-uniform coverage means non-uniform thickness and non-continuous coverage; hence the LM can provide an estimation of the 'effective thickness' (ET) and relative surface coverage using the following:

$$I(\lambda)_{total} = \alpha I(\lambda)_{PDMS} + (1 - \alpha)I(\lambda)_{Subs} \qquad (3)$$

where α is the coverage factor, I_{total} I_{PDMS} and I_{Subs} are the total spectral measurement, PDMS contribution, and reflected intensity of the substrate, correspondingly. It was found that the lab experiment corresponds to 2 μm ET and 2% coverage.

As demonstrated in **Figures 3** and **4** for layers, and in **Figure 5** and Ref. [36] for sprayed traces, the spectral scattering of different ET expresses in non-identical spectral responses, i.e., different peaks heights and locations. **Figure 5** and Ref. [36] exemplify that fitting the best correlated LM result to unknown dissemination results in high certainty identification [36]. Using this approach of forcing the LM over non-uniform coverage, we can circumvent the requirement of the different scattering models to characterize the morphological properties of the analyte and provide identification and also a good estimation of its coverage features.

3. Detection and identification in the SWIR

Although, the absorption spectrum of the invisible range was discovered in 1800 was at the near-infrared (NIR) [37–39], it was almost ignored until the 1950s, as it was not considered for analytical purposes. Spectroscopic investigation of chemicals, for various purposes, was perused in the longer wavelengths, i.e., 7–14 μm, which provides specific information regarding the molecular structure of materials, which are expressed in distinctive narrow absorption peaks. The spectroscopy in the VIS-SWIR range (sometimes referred to as NIR, 800–2500 nm) exhibits broad overlapping peaks resulting from combinations of overtones and transitions in the MWIR. Theoretically, under the assumption of harmonic potential, part of the transitions is forbidden, resulting in low absorption. In the 1950s, SWIR spectroscopy was pushed forward due to technical and analytics progress, i.e., the development of lead sulfide semiconductor detectors and improvement in computing and data analysis techniques—chemometrics [40]. Consequently, this spectral range became more prominent in industry and research, providing rapid, nondestructive measurements for various fields [41, 42]. Another difference between SWIR and MWIR is the increased penetration depth of SWIR which effects the diffusion of the reflected light, as illustrated in **Figure 6**. As seen from the figure, the reflection of light from a solid sample occurs in two forms—specular and diffuse reflection. In contrast to MWIR, which is reflected from the surface, radiation in the SWIR will penetrate the sample and therefore is affected both by absorption and scattering. Various studies utilized this property for the investigation of deeper layers of samples, such as fruits and vegetables having penetration depth between 1 and dozens of microns [43, 44], or near-surface (~1 mm) as in soil [45]. Another advantage of using SWIR is the lack of blackbody radiation from the sample and the high SNR of detectors. For example, among other advantages and
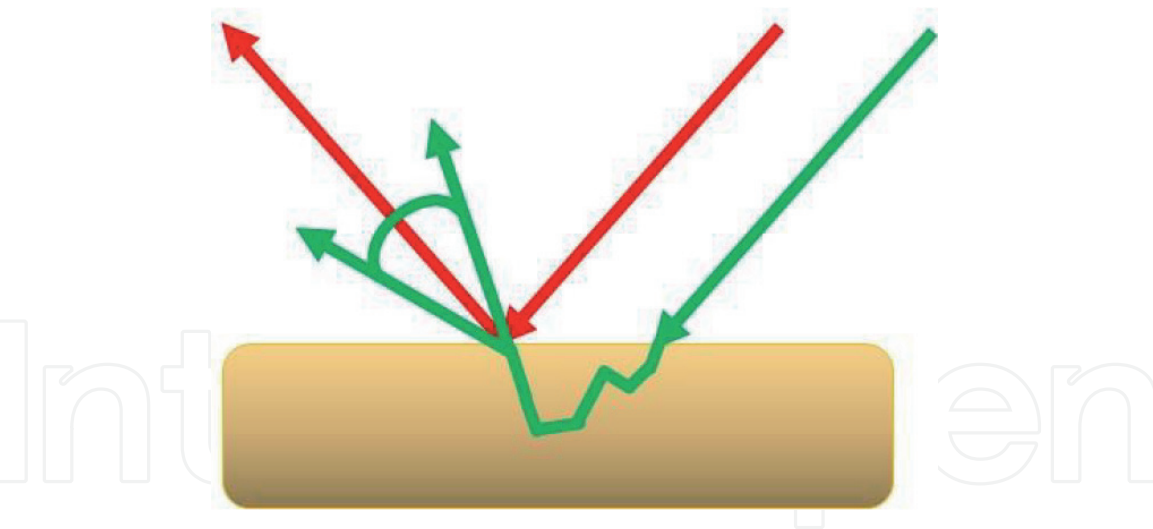
Figure 6.
Reflection measurements—spectral (red) and diffuse (green) reflection. In cases where the beam penetrated the sample, it suffers.

uses of SWIR spectroscopy, Manely indicated the increased penetration depth (compared to the MWIR), that can be utilized to rapidly analyze biological materials such as food products without sample preparation [41].

Reflectance measurements produce a large amount of data that have to be analyzed in real-time. For example, Park et al. utilized reflectance spectroscopy for real-time in-line poultry fecal detection [46]. They placed a dedicated camera to measure the reflectance spectrum in every pixel in the image—a hyperspectral imager (HSI—see **Figure 7**). The HSI was integrated into the production line, so both the data acquisition and interpretation are performed in real-time with no need for exhaustive sample preparation techniques. Similarly, Sendin et al. described the application of SWIR HSI for the quality and safety evaluation of cereals which are an essential part of the global population diet [42]. The HSI measurements can be performed in various scales enabling monitoring of a single grain to detect, for example, fungi, or on a larger scale to determine the overall cereal stock quality. Another area in which spectroscopy in the SWIR gained popularity is geophysical mapping. Goetz, one of the pioneers in this vibrant field of
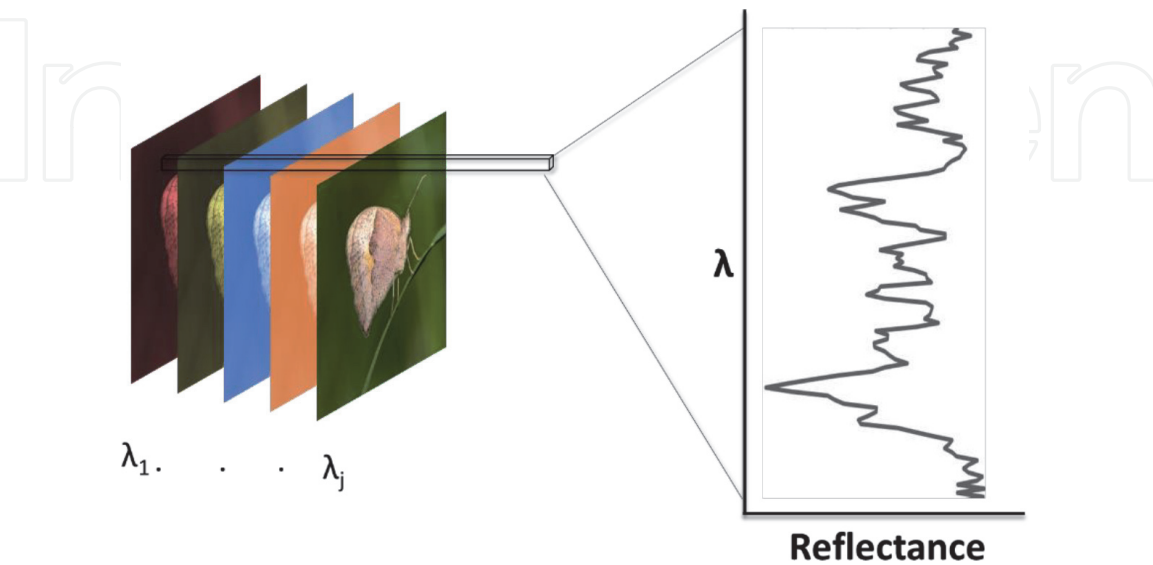

Figure 7.
An illustration of the HSI measurement. A scene is sampled in various wavelengths resulting in multiple images, which are referred to as a data cube. Each pixel in the data cube contains both spatial and spectral information. The right side of the figure shows the reflectance spectrum extracted from a pixel in the upper left corner of the image.

research, recognized the future advantages of imaging remote sensing in the 1980s, for the identification of earth surface materials by their reflectance spectra [47]. For example, Ben-Dor et al. mapped soil properties using air-born HSI in the visible SWIR range (DAIS-7915) [48]. They developed methods to map soil organic matter, soil field moisture, saturated moisture, and soil salinity. These studies and many others utilize the robustness of the spectral measurements in the SWIR. However, two challenges have to be considered; the first one is the atmosphere effect of the reflected light, and the second one is data analysis. Brook and Ben-Dor, developed a calibration technique that utilizes targets placed in the trajectory of the airborne sensor [49]. The calibration process (supervised vicarious calibration—SVC), is performed during the mission and accounts for sensor properties and atmospheric interference.

Data analysis also received significant attention, and several algorithms have been introduced over the years to detect sample anomalies or specific target materials in imaging and non-imaging spectroscopy. Manolakis and Shaw described several algorithms for analyzing HSI data [50]. In general, these algorithms are designed to find indications for a phenomenon of interest. For example, the presence of a specific material that exceeds the naturally occurring variability in the sample, which is to be expected in many real-life applications such as process control, geophysical mapping and other applications in which sample preparation is impractical. Some of these algorithms can resolve common situations in remote sensing, where the target material occupies only a portion of the sampling area, i.e., linear mixing between the reflectance spectrum of the target material and unknown background material. However, in some specific cases, non-linear mixing may also occur since the incoming light might pass through a thin film of one material and then be reflected by the background material that supports this film—"intimate mixing", in which the resulted spectrum is a dot product of the film and the supporting material [51]. Kendler et al. developed an algorithm that automatically resolves non-linear mixing between background and target materials by utilizing the benefits of HSI [23, 52]. The algorithm seeks a pixel without the target material (clear background) having a similar reflectance spectrum supporting the target material (target pixel). Once such clear background is located in the image, the pure spectrum is extracted and compared to a library reference. It was also shown that the quality of extraction of the pure spectrum increases as the physical distance between the clear background and the target pixel decreases [53]. Conversely, in non-imaging spectroscopy, such a process may be impractical. This is exemplified in **Figure 8**, presenting normalized laboratory measurements of commercial granulated sugar and powdered sugar (<125 μm), disseminated over PVC and laminated wood surfaces. The measurements were conducted with a spectrometer (ASD FieldSpec® 4 Hi-Res) at 350–2500 nm using a custom accessory sampling contact probe consisting of a Halogen lamp and a collecting fiber as input. This tabulated figure accentuates the diversity and complexness of SWIR reflectance spectroscopy described above, by presenting significant spectral differences of four different types of measurements of the same chemical. It shows that both the surface and the physical state of the sample affects the reflected spectrum in a way that cannot be eliminated using a simple non-linear unmixing model.

Therefore, it is concluded that utilizing SWIR spectroscopy for a minute amount of material placed on a surface might pose a significant analytical challenge. Although, a simple unmixing model can be applied in some cases, where the background surface is opaque, the sample has low light scattering and absorption, and the measurement is performed using an imaging spectrometer. However, it is hard to guarantee such a set of conditions in many cases that may be ubiquitous in real-life applications.
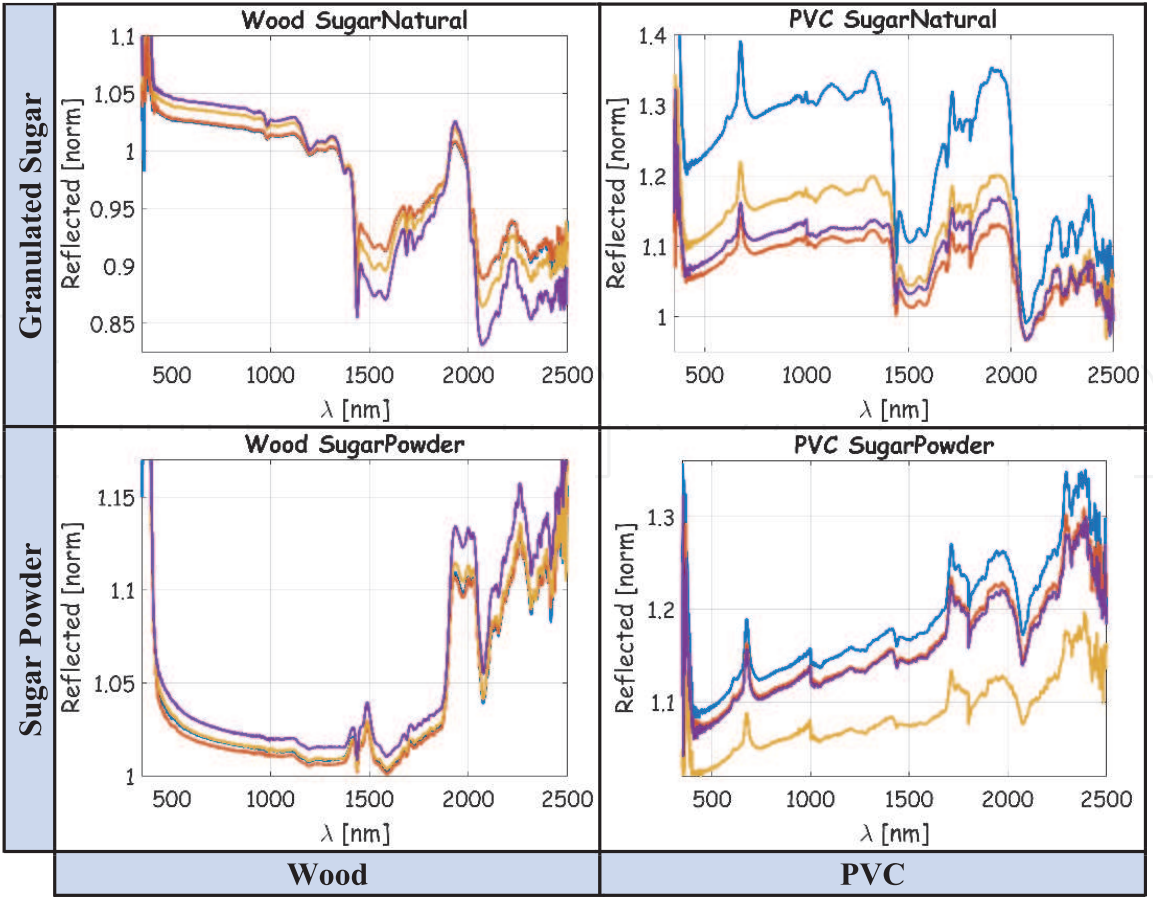
Figure 8.
Diffuse reflectance of sugar (granulated and powdered) on PVC and wood surfaces.

3.1 Classification of powdery residuals

Spectral detection and classification of powdery and condensed materials for security, safety, food industry hygiene, etc., was suggested at various spectral regions, from THz [13, 14, 54, 55] through the MWIR [12, 34, 35], SWIR [56, 57] and more. However, in lower wavelengths (VIS-SWIR), most powders, especially fine-grained powders, appear visually similar and therefore hard to distinguish, have little color and texture, and appear white (due to scattering). Also, the spectral contribution of the carrying surface tends to blend with the powder's spectrum, as discussed above. The literature shows many examples for powders and materials detection and classification, utilizing the availability and low cost of using the visual and near IR ranges for that task. Spectral imaging and computer vision was employed by Zhi, who showed reasonable classification accuracy (60–70%) for discrimination of 100 powders, using three cameras (RGB, NIR, SWIR) and 12 minutes acquisition time [58]. Classification of surfaces materials, also by computer vision, was used by capturing the micro-geometry and reflectance properties of the surfaces, using a photometric stereo sensor with a 3 cm working distance [59]. These examples require expensive light sources or complicated measurement apparatus, despite the use of the visual regime, which is supposed to be cheaper and less complex. This section presents the VIS-SWIR non-imaging spectral measurements and data analysis approach, for powders on various surfaces, with low hardware and software requirements, for powders detection and identification through classification.

3.1.1 Data acquisition and analysis

Different powders (sodium carbonate, Arizona dust, tryptophan, tenax, caffeine, hepes, copper) were disseminated on various surfaces (ceramics, laminated

wood, PCV, cardboard, Perspex, acrylic glass, Teflon, painted and bare car metal, plastics, marble stone, pebble), and their VIS-SWIR spectrum was acquired using a non-imaging spectrometer. The data were collected using a spectrometer (Filedspec4 from ASD, with 2151 sampling points from 350 to 2500 nm) and a sampling contact probe consisting of a Halogen lamp and a collecting fiber as input. For each surface, various measurements were conducted, having different concentrations of powder per unit surface. Thus, a large dataset was collected, comprised of a range of intensities, and different relations between absorption peaks. Another source of spectral diversity is the size, shape, and orientation of the measured particles, which affects their scattering properties. It is worth noticing that due to these scattering effects, the orientation (pivot) of the surface also affects its reflected spectrum. These measurements produce a diverse dataset, well suitable for statistical learning methods, aka machine learning.

Supervised learning (classification) is the process of predicting the category of a given data point, based on a label train-set. The learning algorithm is supplied with a labeled train-set, in which every measurement is labeled in advance and learns the mapping function between the new input data and its response (label). Some data sets are linearly separable, and can be processed with linear algorithms such as SVM (support vector machine), while other problems require a higher-order hyper-plane to resolve the data. Applying some effort (such as kernel methods) enables linear learning algorithms to learn non-linear decision boundaries. Another approach to 'upgrade' simple algorithm performance is ensemble learning, in which weak learners are ensemble together to provide predictions that outperform the use of a single type of these learners, and to learn more complicated decision boundaries. One of these algorithms is random forest (RF, also known as tree bagger), which uses classification trees [60] and bootstrap aggregation random processes. The RF algorithm is trained using ~70% of the data (training set), and the produced model is tested on the rest of the unseen data (test-set). On the train set data, RF performs a process of bootstrap aggregation (bagging) in which a subset of the train set (2/3) is randomly picked iteratively to produce a classification model whose results are examined on the rest third of the data- the validation set. This random process, and the random selection of predictors at each tree node, decrease the variance errors and enable the production of another measurement of the predictor—the "out-of-bag error" (OOBerr). By comparing the errors produced with and without each predictor, the OOBerr scores each predictor to note its contribution to the learning process. For further reading about RF, see Breiman [61–62].

Figure 9 presents the confusion matrix[1] presenting the classification results of the aforementioned powders and surfaces, showing total accuracy of almost 90%, and high true positive rates (TPR, noted in the right vertical column). Note that the presented powders appeared white and indistinctive to the human eye, except copper that is in the form of metallic reddish flattened flakes. Nonetheless, all powders (except tryptophan) were classified with a similar TPR. The measurements are not normalized by the surface signature, exemplifying the strength of the classification process, which learns to ignore the distracting influence of the carrying surface.

As explained, the OOBerr parameter evaluates the contribution of each predictor (i.e., wavelength) to the learning process. By using only some of the top influencers, it is possible to avoid bad predictors, and reduce the required data volume, thus

---

[1] The confusion matrix compares the true class with the predicted class for each class. The diagonal terms represent the true classification, and its ratio to the total matrix represents the accuracy.
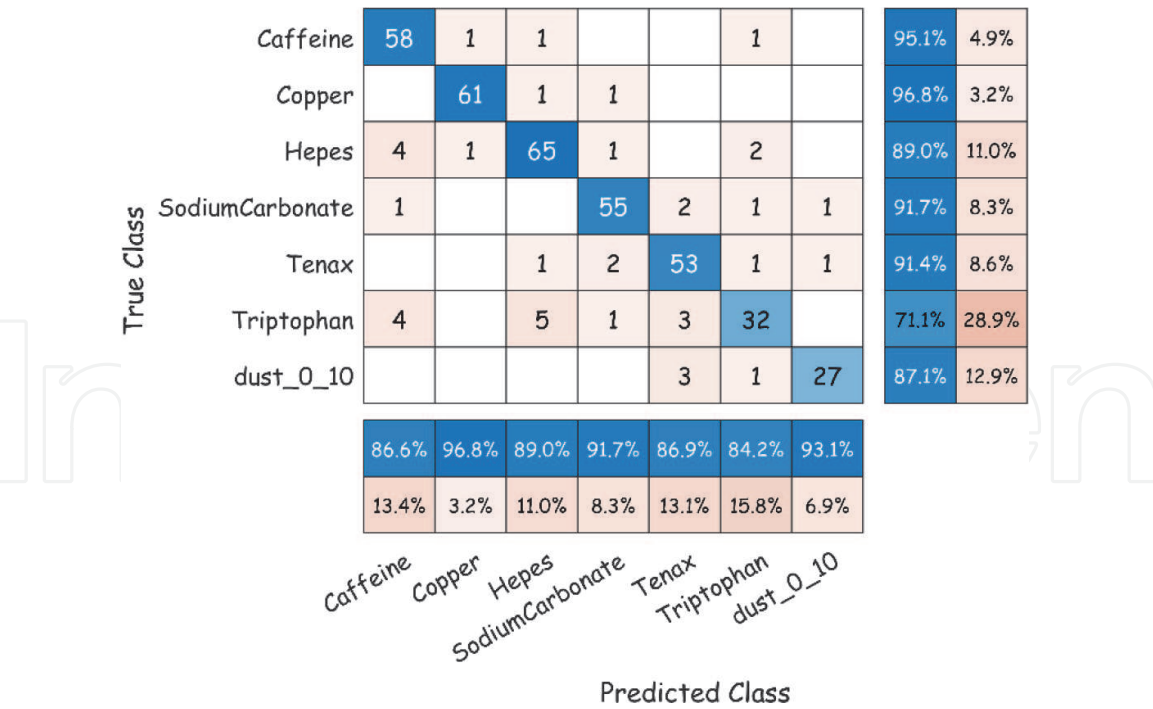
Figure 9.
Confusion matrix—classification of powders on surfaces, using hyper-spectral data.

speeding the whole process. **Figure 10b** illustrates the importance of all 2151 predictors from the OOBerr computation, where the top 5% are marked in black. The confusion matrix in **Figure 10b** shows RF classification with these 108 selected features. We see that the classification performance is almost unchanged, and the accuracy has an insignificant decrease of 0.4%.

3.2 Application: classification of wheat yellow rust disease

Wheat is one of the world's major crops and provides a substantial amount of starch, proteins, vitamins, and dietary calories worldwide. One of the major threats, on a global scale, to wheat production is Yellow Rust (YR) disease, which is the most damaging disease of wheat on a global scale and causes an annual loss of millions of tons of wheat harvest valued at around 1G USD. Due to global warming and the evolution of YR strains adapted to higher temperatures, YR damages wheat crops in areas where it had not been previously reported. The spores are carried with the winds and reaches high altitudes so it can travel long distances. YR has a complex life cycle that includes several hosts and spore stages, which eventually appear as yellow particles (size of a few dozens of microns) covering the leaf surface, as seen in **Figure 11** left. Managing yellow rust can be utilized through the application of fungicides [63, 64], using resistant plants [65], and tracking [66]. While using resistant varieties is an efficient strategy, it poses some challenges for YR detection for two main reasons: (1) co-evolution of the host wheat and the fungal pathogen, might enable YR to overcome the YR-resistant genes mechanism. Hence, resistant plants also need monitoring for disease detection. (2) The Hypersensitive Response (HR) of a resistant leaf appears to be visually similar to YR disease. This is exemplified in **Figure 11** (right), presenting HR and YR early stages, which are visually hard to discriminate. This situation resembles the above-described detection of powder on a carrying surface, where the surface is the green leaf, and the powder is the powdery particle of YR spores. Therefore, applying similar measurements and data processing methods can successfully classify the disease stages and HR response for the early detection of YR in the field.
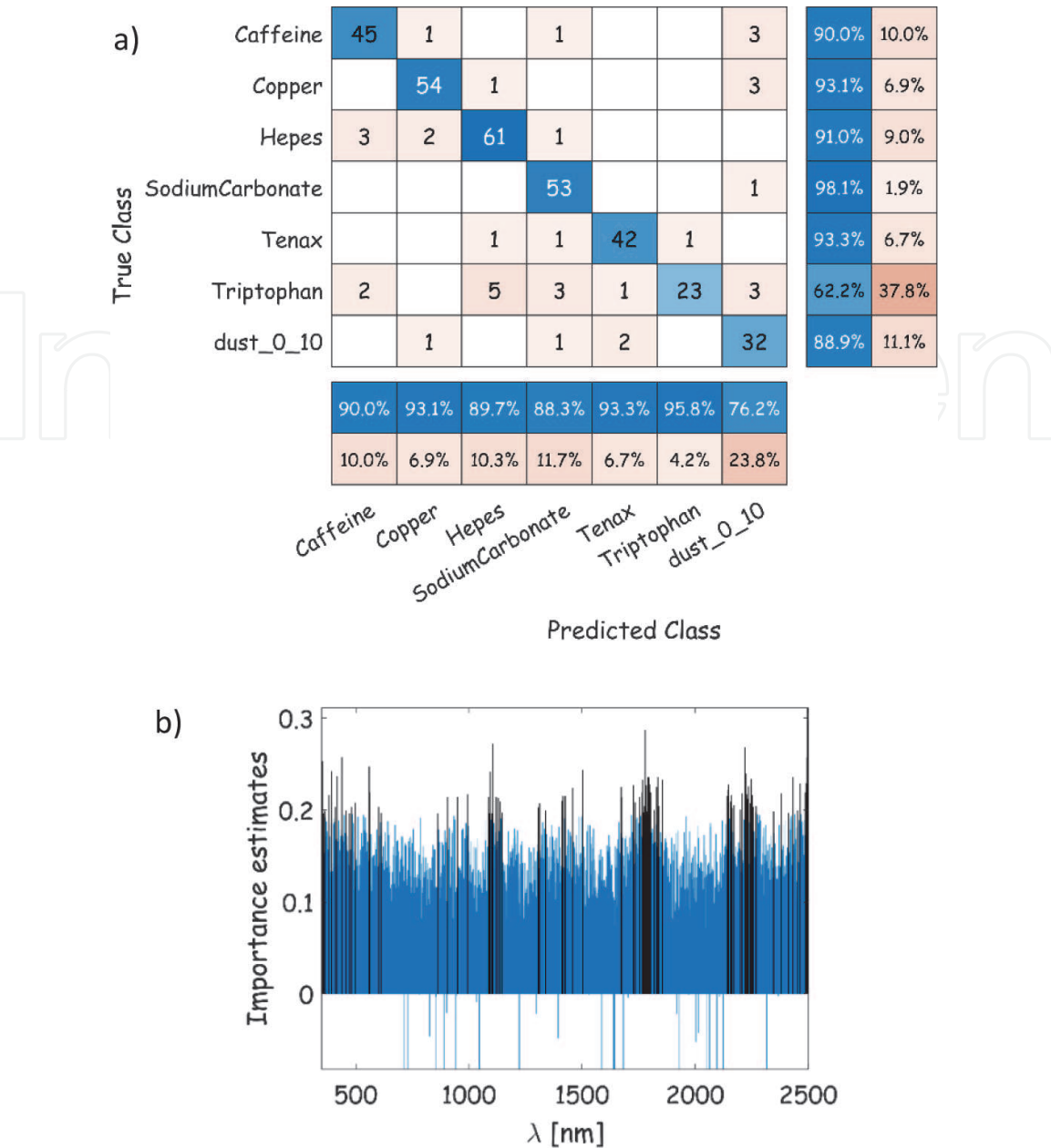
Figure 10.
(a) Confusion matrix—classification of powders on surfaces, using top 5% important predictors presented in (b).
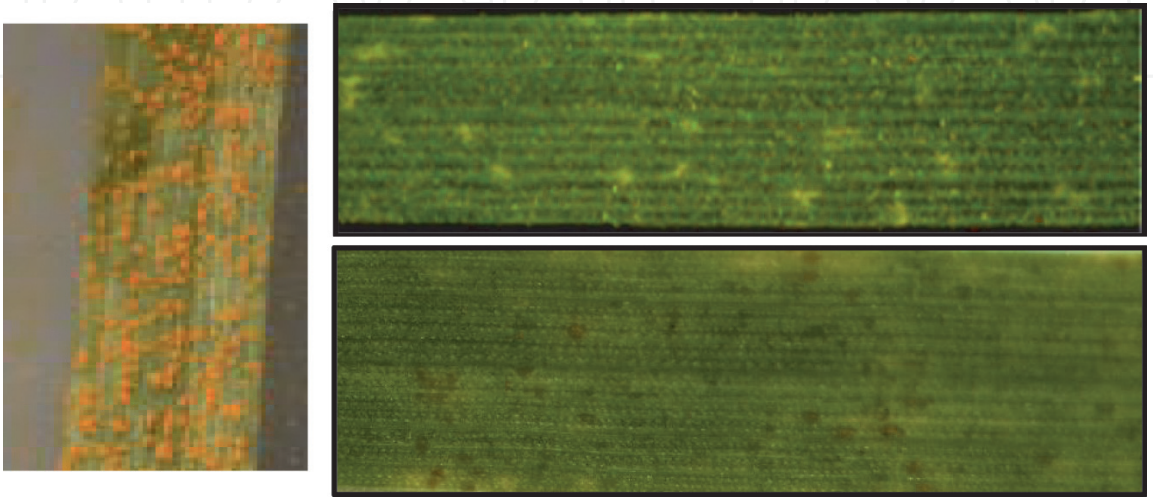

Figure 11.
YR symptoms on susceptible and resistant wheat leaves. Left—fully developed YR. Right: resistant (top) and susceptible (bottom) wheat leaves response to YR. The top leaf exhibits HR symptoms, which is visually similar to YR early symptoms in the lower leaf.
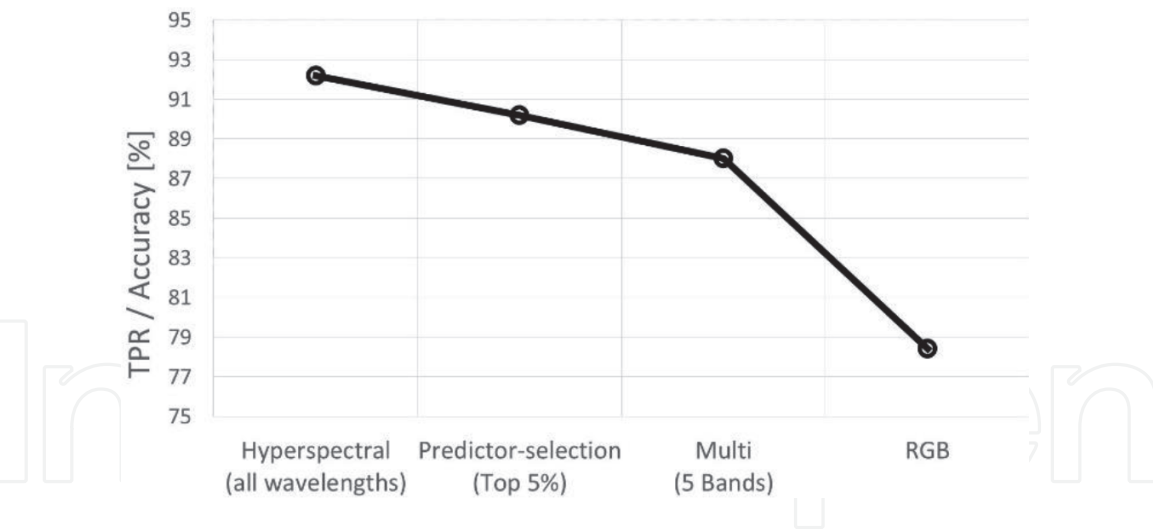
Figure 12.
True positive rates (TPR) of early stages of sporulation vs. four levels of the predictors set: hyperspectral (all 2151 wavelengths), predictor-selection (top 5% important); multi-spectral (5-bands), and RGB.

Figure 12 illustrates the results of the classification process. The VIS-SWIR spectrum of hundreds of wheat leaves in various stages was acquired and classified with RF. Some of the leaves were green and healthy, some susceptible to YR, exhibiting sporulation in several stages (from the onset of sporulation; sporulation early stages; final sporulation stages), and some resistant leaves exhibiting several stages of HR (early stages and fully developed HR). The figure presents the TPR of sporulation early stages at four different data dimensions. Using all 2151 predictors produces a TPR of 92.2%. Using the feature selection process described in the previous section produced a slight decrease (TPR of 90.2%), using only 108 predictors. Further directionality reduction to five spectral bands (conventional agricultural imager) results in a TPR of 88%. Using only RGB channels results in a TPR of 78.4%. This noteworthy result pledges that YR detection does not require expensive specific hardware, and enables on-site monitoring by non-experts.

4. Summary/conclusions

Spectral light reflection can be used for the identification of particulate and condensed chemicals. In controlled situations, such as laboratory measurements, the sample can be manipulated to provide consistent high-quality reflectance spectra that can be used to characterize and identify the sample at hand. Such manipulations involve classical sample treatment techniques such as purification, grinding, and pressing to a pellet. However, standoff sensing of un-manipulated samples results in noisy measurements, requiring more sophisticated data analysis to extract meaningful information. LWIR spectrum does contain specific, unambiguous information of the molecular structure, but it involves scattering phenomena that require an adapted model, accounting for the sample's physical geometrical properties. A simple unified model was suggested to bypass this issue using a simplified model. A different analysis method was demonstrated in the case of light scattering in the SWIR. In this case, the reflectance spectra are broader and weaker, and a machine-learning model is used to classify the sample according to its typical reflectance. An additional consequence of the machine-learning model is the assessment of the contribution of each wavelength to the accuracy of the classification. Using only the important wavelength can speed up the computation and simplify the measurement, thus enhancing the usability of reflectance spectroscopy.

List of abbreviations

ATR	attenuated total reflection
EC-QCL	external-cavity quantum cascade laser
ET	effective thickness
FTIR	Fourier transform infra-red (spectroscopy)
HIS	hyperspectral imager
HR	hypersensitive response
IR	infra-red
LM	layers model
NIRMWIR/SWIR	near/mid/short wave infrared
OOBerr	out-of-bag error
PDMS	poly-dimethyl-siloxane
PMMA	polymethyl methacrylate
PVC	polyvinyl chloride (polymer)
QCL	quantum cascade laser
RF	random forest
RGB	red, green, blue
SNR	signal-to-noise ratio
SVM	support vector machine
TPR	true positive rate
VIS	visual (visual spectral range)
YR	yellow rust

Author details

Ran Aharoni[1]*, Asaf Zuck[2], David Peri[3] and Shai Kendler[1,4]

1 Department of Environmental Physics, Israel Institute for Biological Research, Ness-Ziona, Israel

2 Department of Chemical Physics, Israel Institute for Biological Research, Ness-Ziona, Israel

3 Independent Scientist, Israel

4 Faculty of Civil and Environmental Engineering, Water and Agricultural Engineering, Technion—Israeli Institute of Technology, Haifa, Israel

*Address all correspondence to: tenzoran@gmail.com

IntechOpen

References

[1] Van Neste CW, Senesac LR, Thundat T. Standoff spectroscopy of surface adsorbed chemicals. Analytical Chemistry. 2009;**81**(5):1952-1956

[2] Aharoni R, Klymiuk V, Sarusi B, Young S, Fahima T, Fishbain B, et al. Spectral light-reflection data dimensionality reduction for timely detection of yellow rust. Precision Agriculture. 2020;**22**:267-286. DOI: 10.1007/s11119-020-09742-2

[3] Staymates JL, Staymates ME, Lawrence J. The effect of reusing wipes for particle collection. International Journal for Ion Mobility Spectrometry. 2015;**19**(1):41-49

[4] Garcia-Reyes JF, Harper JD, Salazar GA, Charipar NA, Ouyang Z, Cooks RG. Detection of explosives and related compounds by low-temperature plasma ambient ionization mass spectrometry. Analytical Chemistry. 2010;**83**(3): 1084-1092

[5] Justes DR, Talaty N, Cotte-Rodriguez I, Cooks RG. Detection of explosives on skin using ambient ionization mass spectrometry. Chemical Communications. 2007;**21**:2142-2144

[6] He J, Tang F, Luo Z, Chen Y, Xu J, Zhang R, et al. Air flow assisted ionization for remote sampling of ambient mass spectrometry and its application. Rapid Communications in Mass Spectrometry. 2011;**25**(7):843-850

[7] Serrano J, Moros J, Sánchez C, Macías J, Laserna JJ. Advanced recognition of explosives in traces on polymer surfaces using LIBS and supervised learning classifiers. Analytica Chimica Acta. 2014;**806**:107-116

[8] Tourne M. Developments in explosives characterization and detection. Journal of Forensic Research. 2014;**S12**:002. DOI: 10.4172/2157-7145. S12-002

[9] Li H, Tripp CP. Detection of Bacillus globigii spores using a fourier transform infrared-attenuated total reflection method. Applied Spectroscopy. 2008; **62**(9):963-967

[10] Andrew Chan KL, Kazarian SG. Detection of trace materials with Fourier transform infrared spectroscopy using a multi-channel detector. The Analyst. 2006;**131**(1):126-131

[11] Harig R, Braun R, Dyer C, Howle C, Truscott B. Short-range remote detection of liquid surface contamination by active imaging Fourier transform spectrometry. Optics Express. 2008;**16**(8):5708

[12] Braun R, Harig R. Stand-off identification and mapping of liquid surface contaminations by passive hyperspectral imaging. Chemical, Biological, Radiological, Nuclear, and Explosives Sensing XIV. 2013;**8710**: 871004

[13] Dobroiu A, Sasaki Y, Shibuya T, Otani C, Kawase K. THz-wave spectroscopy applied to the detection of illicit drugs in mail. Proceedings of the IEEE. 2007;**95**(8):1566-1575

[14] Wang S, Ferguson B, Mannella C, Abbott D, Zhang X-C. Powder detection using THz imaging. In: Summaries of Papers Presented at the Quantum Electronics and Laser Science Conference. America: Opt. Soc.; 2002. p. 44

[15] Patel CKN. From CO_2 lasers to quantum cascade lasers—A saga of high power infrared lasers. Journal of Laser Applications. 2010;**21**(4):224-238

[16] Tittel FK, Richter D, Fried A. Mid-infrared laser applications in spectroscopy. Solid-State Mid-Infrared Laser Sources. 2007;**516**(7):458-529

[17] Chen X, Guo D, Choa F-S, Wang C-C, Trivedi S, Snyder AP, et al. Standoff photoacoustic detection of explosives using quantum cascade laser and an ultrasensitive microphone. Applied Optics. 2013;**52**(12):2626

[18] Patel CKN, Barron-Jimenez R, Dunayevskiy I, Tsvid G, Lyakh A. Two wavelength operation of an acousto-optically tuned quantum cascade laser and direct measurements of quantum cascade laser level lifetimes. Applied Physics Letters. 2017;**110**:031104. DOI: 10.1063/1.4974214

[19] Craig IM, Taubman MS, Lea AS, Phillips MC, Josberger EE, Raschke MB. Infrared near-field spectroscopy of trace explosives using an external cavity quantum cascade laser. Optics Express. 2013;**21**(25):30401

[20] Phillips MC, Bernacki BE. Hyperspectral microscopy of explosives particles using an external cavity quantum cascade laser. Optical Engineering. 2012;**52**(6):061302

[21] Goyal AK, Wood D, Lee V, Rollag J, Schwarz P, Zhu L, et al. Laser-based long-wave-infrared hyperspectral imaging system for the standoff detection of trace surface chemicals. Optical Engineering. 2020;**59**(09):1

[22] Pavlenko AA, Maksimenko EV, Chernyshova LV. Stand-off detection of HMX traces by active spectral imaging with a tunable CO_2 laser. Quantum Electronics. 2014;**44**(4):383-386

[23] Kendler S, Aharoni R, Cohen S, Raich R, Weiss S, Levy H, et al. Non-contact and non-destructive detection and identification of *Bacillus anthracis* inside paper envelopes. Forensic Science International. 2019;**301**:e55-e58

[24] Yang J, Messinger DW. Bloodstain detection and discrimination impacted by spectral shift when using an interference filter-based visible and near-infrared multispectral crime scene imaging system. Optical Engineering. 2018;**57**(03):1

[25] Stenzel O. The Physics of Thin Film Optical Spectra: An Introduction (Springer Series in Surface Sciences). 2nd ed. Vol. 44. Cham: Springer International Publishing; 2016. 1-352 p

[26] Yariv A. Quantum Electronics. 3rd ed. New York: Wiley; 2020. Available from: Wiley.com

[27] Kovalenko SA. Descartes-Snell law of refraction with absorption. Semiconductor Physics, Quantum Electronics and Optoelectronics. 2001;**4**(3):214-218

[28] Mugele RA, Evans HD. Droplet size distribution in sprays. Industrial and Engineering Chemistry. 1951;**43**(6):1317-1324

[29] Kippax P, Parkin S, Tuck C. Particle size characterisation of agricultural sprays using laser diffraction. ILASS-Europe. 2002;**6**(2):2-7

[30] Patterson MA, Reitz RD. Modeling the effects of fuel spray characteristics on diesel engine combustion and emission. In: SAE Technical Papers. SAE International; 1998

[31] Mishchenko MI. Maxwell's equations, radiative transfer, and coherent backscattering: A general perspective. Journal of Quantitative Spectroscopy and Radiation Transfer. 2006;**101**(3):540-555

[32] Wriedt T. Mie theory: A review. In: Springer Series in Optical Sciences. Berlin, Heidelberg: Springer; 2012. pp. 53-71

[33] Young AT. Rayleigh scattering. Physics Today. 1982;**35**(1):42-48

[34] van de Hulst HC. Light Scattering by Small Particles (Dover Books on

Physics). 2nd ed. New York: Dover Publications; 1981. 496 p

[35] Bohren CF. Scattering by a sphere and reflection by a slab: Some notable similarities. Applied Optics. 1988;**27**(2): 205

[36] Aharoni R, Elisha S, Peri D, Kendler S. Liquid trace detection and identification by spectral reflectance model. Optical Engineering. 2019; **58**(07):1

[37] Herschel W. XIV. Experiments on the refrangibility of the invisible rays of the sun. Philosophical Transactions. Royal Society of London. 1800;**90**: 284-292

[38] Herschel W. XIII. Investigation of the powers of the prismatic colours to heat and illuminate objects; with remarks, that prove the different refrangibility of radiant heat. To which is added, an inquiry into the method of viewing the sun advantageously, with telesco. Philosophical Transactions. Royal Society of London. 1800;**90**: 255-283

[39] Herschel W. XV. Experiments on the solar, and on the terrestrial rays that occasion heat; with a comparative view of the laws to which light and heat, or rather the rays which occasion them, are subject, in order to determine whether they are the same, or different. Philosophical Transactions. Royal Society of London. 1800;**90**:293-326

[40] Adams MJ. Chemometrics in Analytical Spectroscopy (RSC Analytical Spectroscopy Series). Cambridge: Royal Society of Chemistry; 2007

[41] Manley M. Near-infrared spectroscopy and hyperspectral imaging: Non-destructive analysis of biological materials. Chemical Society Reviews. 2014;**43**(24): 8200-8214

[42] Sendin K, Williams PJ, Manley M. Near infrared hyperspectral imaging in quality and safety evaluation of cereals. Critical Reviews in Food Science and Nutrition. 2018;**58**(4):575-590

[43] Qin J, Lu R. Measurement of the optical properties of fruits and vegetables using spatially resolved hyperspectral diffuse reflectance imaging technique. Postharvest Biology and Technology. 2008;**49**(3):355-365

[44] Lammertyn J, Peirs A, De Baerdemaeker J, Nicolaï B. Light penetration properties of NIR radiation in fruit with respect to non-destructive quality assessment. Postharvest Biology and Technology. 2000;**18**(2):121-132

[45] Norouzi S, Sadeghi M, Liaghat A, Tuller M, Jones SB, Ebrahimian H. Information depth of NIR/SWIR soil reflectance spectroscopy. Remote Sensing of Environment. 2021;**256**: 112315

[46] Park B, Yoon S-C, Windham WR, Lawrence KC, Kim MS, Chao K. Line-scan hyperspectral imaging for real-time in-line poultry fecal detection. Sensing and Instrumentation for Food Quality and Safety. 2011;**5**(1):25-32

[47] Goetz AFH, Vane G, Solomon JE, Rock BN. Imaging spectrometry for Earth remote sensing. Science (80-). 1985;**228**(4704):1147-1153

[48] Ben-Dor E, Patkin K, Banin A, Karnieli A. Mapping of several soil properties using DAIS-7915 hyperspectral scanner data—A case study over soils in Israel. International Journal of Remote Sensing. 2002;**23**(6): 1043-1062

[49] Brook A, Dor E. Ben. Supervised vicarious calibration (SVC) of hyperspectral remote-sensing data. Remote Sensing of Environment. 2011; **115**(6):1543-1555

[50] Manolakis D, Shaw G. Detection algorithms for hyperspectral imaging applications. IEEE Signal Processing Magazine. 2002;**19**(1):29-43

[51] Bioucas-Dias JM, Plaza A, Dobigeon N, Parente M, Du Q, Gader P, et al. Hyperspectral unmixing overview: Geometrical, statistical, and sparse regression-based approaches. IEEE Journal of Selected Topics in Applied Earth Observations and Remote Sensing. 2012;**5**(2):354-379

[52] Kendler S, Ron I, Cohen S, Raich R, Mano Z, Fishbain B. Detection and identification of sub-millimeter films of organic compounds on environmental surfaces using short-wave infrared hyperspectral imaging: Algorithm development using a synthetic set of targets. IEEE Sensors Journal. 2019;**19**(7):2657-2664

[53] Hollis J, Raich R, Kim J, Fishbain B, Kendler S. Foreground signature extraction for an intimate mixing model in hyperspectral image classification. In: ICASSP 2020—2020 IEEE International Conference on Acoustics, Speech and Signal Processing (ICASSP). IEEE; 2020. pp. 4732-4736

[54] Sengupta A, Bandyopadhyay A, Barat RB, Gary DE, Federici JF. THz reflection spectroscopy of C-4 explosive and its detection through interferometric imaging. In: Hwu RJ, Linden KJ, editors. Proc. SPIE. Terahertz and Gigahertz Electronics and Photonics V. Vol. 6120. 2006. p. 61200A. DOI: 10.1117/12.641727

[55] Deutsch ER, Kotidis P, Zhu N, Goyal AK, Ye J, Mazurenko A, et al. Active and passive infrared spectroscopy for the detection of environmental threats. Advanced Environmental, Chemical, and Biological Sensing Technologies XI. 2014;**9106**:91060A

[56] Kendler S, Aharoni R, Cohen S, Raich R, Weiss S, Levy H, et al. Non-contact and non-destructive detection and identification of *Bacillus anthracis* inside paper envelops. Forensic Science International. 2019;**301**:e55-e58. DOI: 10.1016/j.forsciint.2019.05.007

[57] Nelson MP, Shi L, Zbur L, Priore RJ, Treado PJ. Real-time short-wave infrared hyperspectral conformal imaging sensor for the detection of threat materials. In: Fountain AW, editor. Chemical, Biological, Radiological, Nuclear, and Explosives (CBRNE) Sensing XVII. International Society for Optics and Photonics; 2016. p. 982416

[58] Zhi T, Pires BR, Narasimhan SG. Multispectral imaging for fine-grained recognition of powders on complex backgrounds. In: 2019 IEEE/CVF Conference on Computer Vision and Pattern Recognition (CVPR). 2019. pp. 8691-8700. DOI: 10.1109/CVPR.2019.00890

[59] Kampouris C, Zafeiriou S, Ghosh A, Malassiotis S. Fine-grained material classification using micro-geometry and reflectance. In: Leibe B, Matas J, Sebe N, Welling M, editors. Computer Vision—ECCV 2016. Lecture Notes in Computer Science. Vol. 9909. Cham: Springer; 2016. pp. 778-792. DOI: 10.1007/978-3-319-46454-1_47

[60] Breiman L, Friedman J, Stone C, Olshen R. Classification and Regression Trees. Routledge; 1984. DOI: 10.1201/9781315139470

[61] Breiman L. Bagging predictors. Machine Learning. 1996;**24**(2):123-140

[62] Breiman L. Random forests. Machine Learning. 2001;**45**(1):5-32. DOI: 10.1023/A:1010933404324

[63] Reiss A, Jørgensen LN. Biological control of yellow rust of wheat (*Puccinia striiformis*) with Serenade® ASO (*Bacillus subtilis* strain QST713). Crop Protection. 2017;**93**:1-8

[64] Basandrai A, Sharma B, Basandrai D. Efficacy of triazole fungicides for the integrated management of yellow rust, leaf rust and powdery mildew of wheat. Plant Disease Research. 2013;**28**(2): 135-139

[65] Klymiuk V, Yaniv E, Huang L, Raats D, Fatiukha A, Chen S, et al. Cloning of the wheat Yr15 resistance gene sheds light on the plant tandem kinase-pseudokinase family. Nature Communications. 2018;**9**:3735. DOI: 10.1038/s41467-018-06138-9

[66] A Global Wheat Rust Monitoring System. Available from: RustTracker. org [cited 2021 Sep 13]